Nanoscale

PAPER

View Article Online
View Journal | View Issue

Cite this: *Nanoscale*, 2026, **18**, 3365

Dual pH-responsive pseudopeptide: hydrogelation and self-assembly into single- and multi-walled nanotubes

Arturo Blanco-Gómez, *[a,b] Liliana Barravecchia,[b] Erica Scarel, [a] Rita De Zorzi, [a] Laura Colomina-Alfaro, [c] Antonella Bandiera, [c] Slavko Kralj, [d,e] Alejandro Vila,[b] Davide Porrelli, [c] Carlos Peinador, [b] Marcos D. García *[b] and Silvia Marchesan *[a]

This work reports the heterochiral tripeptide L-Phe-D-Phe-L-Phe, N-capped with vermellogen, as an ionizable pseudopeptide hydrogelator, and how the pH-responsiveness is transferred from the molecular to the nanoscale, and all the way up to the macroscale through self-assembly. In particular, the protonation of the vermellogen moiety is responsible for hydrogelation, while that of the peptide fine-tunes the matrix nanostructure and viscoelastic properties. Electron microscopy reveals the correlation of varying viscoelastic properties with the nanostructure of the hydrogel matrices. Self-assembly of the pseudopeptide undergoes a peculiar evolution from nanofibers to nanotubes. This process depends on the degree of C-terminal deprotonation, notably with the gradual increase in the internal diameter of the resulting nanotubes as the deprotonation progresses to completion. State-of-the-art characterization techniques confirm that the nanostructured gels are predominantly comprised of parallel β-sheets as primary self-assembling motifs, arranging vermellogen units in a clockwise helical pattern, which minimizes electrostatic repulsions. The evolution from nanofibers to nanotubes appears to be driven by a long-range hydrogen bonding interaction, involving the hydrazone group and the deprotonated C-terminus of adjacent β-sheets. The potential biomedical application of the gels is demonstrated through the controlled release of a model anticancer drug, and *in vitro* cytocompatibility assays.

Received 26th September 2025,
Accepted 5th January 2026

DOI: 10.1039/d5nr04076k

rsc.li/nanoscale

1. Introduction

Supramolecular hydrogels are exceptionally versatile materials with a wide range of biomedical applications.[1–3] Among the different types of gelators, low-molecular-weight peptides (LMWP) have emerged as excellent candidates for the task, due to their high biocompatibility, low synthetic cost, and ease of modification.[4–6] Due to this accessible structural diversity, LMWPs can robustly self-assemble into various secondary structures through multiple non-covalent interactions (hydrogen bonding, hydrophobic and π–π interactions, *etc.*), typically resulting in nanofibers that form a three-dimensional network able to encapsulate significant amounts of water molecules, creating dynamic hydrogel matrices of high applicative value.[7–13] One of the simplest and most notable examples of LMWP gelling motifs is diphenylalanine (**FF**), the Alzheimer's β-amyloid structural motif.[14] Indeed, even small structural variations of **FF** enable self-assembly into diverse nanomorphologies, such as nanotubes, nanofibers, or nanowires,[15] with useful properties in drug delivery, biosensing, printing, or the development of semiconductors.[16–18] Furthermore, the heterochirality of D-Phe-L-Phe (**fF**) enables control over hierarchical assembly, yielding homogeneously sized nanotubes as opposed to heterogeneous microtubes.[19]

In this context, the synthetic accessibility and dynamic nature of peptide self-assembly has spurred in recent years the introduction of molecular switches (**MS**s) into LMWP gelators, aimed at the development of "smart materials" for man-controlled functions.[20,21] The incorporation of photo- or redox-**MS**s has been used to control the supramolecular organization, stiffness, or functionality of gels in several examples.[22–24] However, most of these **MS**-LMWPs show serious limitations for their application in aqueous media, due

[a]*Chem. Pharm. Sc. Dept., University of Trieste, 34127 Trieste, Italy. E-mail: arturo.blanco.gomez@udc.es, smarchesan@units.it*
[b]*Interdisc. Ctr. Chem. & Biol. (CICA) and Chemistry Dept., Faculty of Science, University of Coruña, 15071 A Coruña, Spain. E-mail: marcos.garcia1@udc.es*
[c]*Life Science Dept., University of Trieste, 34127 Trieste, Italy*
[d]*Materials Synthesis Dept., Jožef Stefan Institute, 1000 Ljubljana, Slovenia*
[e]*Dept. of Pharmaceutical Technology, Faculty of Pharmacy, University of Ljubljana, 1000 Ljubljana, Slovenia*

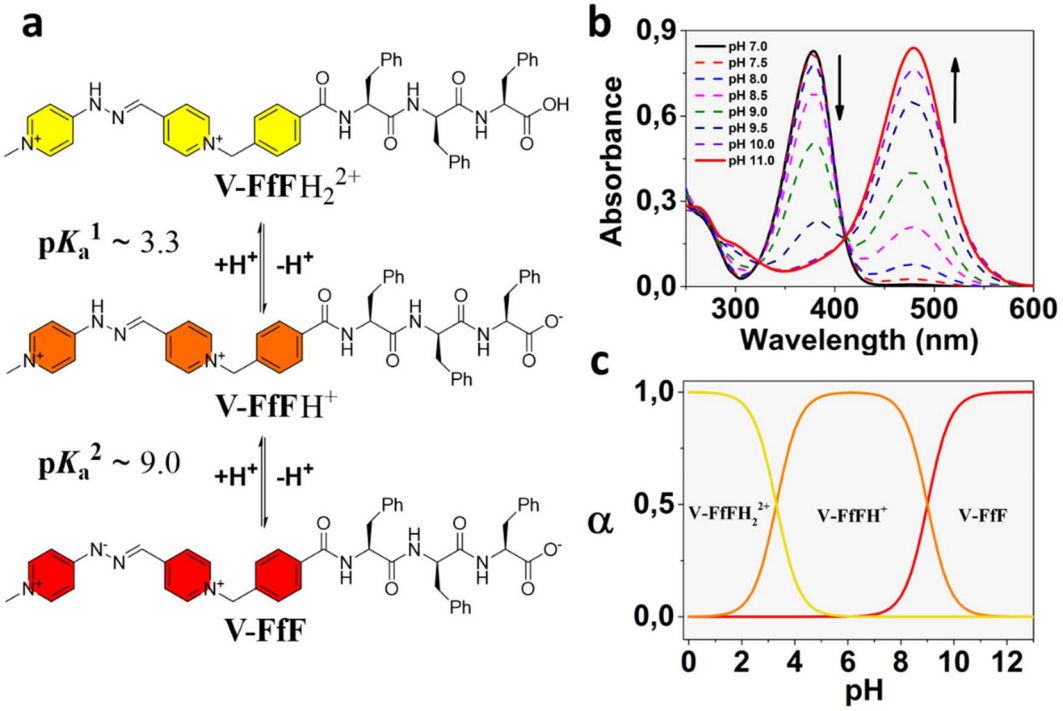

Fig. 1 (a) Schematic depiction of the **V-FfF**H_2^{2+} structure with the corresponding acid–base equilibria. (b) Determination of pK_a^2 by UV-vis titration of **V-FfF**H_2·2Cl at 20 μM in different buffer solutions. (c) Speciation diagram of **V-FfF**H_2^{2+} obtained from the experimental values of pK_a^1 and pK_a^2.[44]

to low solubility or issues of biological incompatibility. One prominent exception to this trend is the control of self-assembly with pH,[25] as the inherent presence of ionizable groups in natural amino acids provides the possibility to control their supramolecular behavior *via* pH modulation,[26–30] yielding ideal platforms for instance for the targeted release of chemotherapeutics, by exploiting the relatively low pH of tumors compared to healthy tissues.[31,32] Nevertheless, exploring the introduction of additional well-defined pH-**MS**s into LMWPs would be highly desirable, in an effort to broaden the pH gelation window, and to allow for the introduction of new chemical properties into these soft materials without interfering with their, otherwise robust, self-assembly.

Recently, some of us reported the development of a new family of bispyridinium-based pH-**MS**s termed "vermellogens" ($\mathbf{VH}^{2+}$),[33–36] which are non-toxic structural analogues of viologens that turn the well-known nature of redox-**MS**s of the latter into the pH-responsiveness at biologically-relevant conditions of the former. This property is attained through the deprotonation of highly delocalized hydrazone groups on the vermellogen unit (pK_a ~ 8–12).[37] This moiety can be easily implemented in solid-phase peptide synthesis,[38] to combine the pH-responsiveness of vermellogens with the gelation properties of short peptides and give access to multi-functional gelators with wide pH-responsiveness and tuneability. In particular, the use of minimalistic heterochiral peptides based on phenylalanine is particularly attractive to yield nanostructured hydrogels with potential biomedical applications, thanks to their good cytocompatibility, and the additional advantage of increased resistance against enzymatic degradation.[39–42]

Consequently, in the work presented herein, we envisioned the development of a novel pH-responsive pseudopeptide (**V-FfF**H_2·2Cl, Fig. 1(a)) with the key structural motifs of a cationic vermellogen ($\mathbf{VH}^{2+}$) and a heterochiral triphenylalanine gelling sequence (**FfF**H), known for adopting a β-sheet-like structure.[43] The aim of the present study is to assert the effect of the two ionizable groups with accessible pK_as on the pH-dependent capabilities of **V-FfF**H_2·2Cl as hydrogelator. As we will show, this pH-**MS** not only increases the typical pH window for LMWP gelification, but also controls both the spontaneous reversible assembly/disassembly of the material and its nanostructuration.

2. Results and discussion

2.1. Molecular characterization of the pseudopeptide V-FfFH_2·2Cl

The pseudopeptide **V-FfF**H_2·2Cl (Fig. 1(a)) was prepared by solid-phase peptide synthesis, and subsequently purified by reversed-phase high-performance liquid chromatography (HPLC), yielding the compound **V-FfF**H_2·2TFA (trifluoroacetate, TFA, as counterion). This salt was characterized by mono- and bi-dimensional nuclear magnetic resonance (1D/2D NMR) techniques, and electrospray-ionization mass spectrometry (ESI-MS), as shown in the SI Section S4. Considering the

well-known ability of the hydrazone group of vermellogens to interact with hydrogen bond acceptor molecules,[37] we performed the metathesis of **V-FfFH$_2$**·2TFA to chloride with HCl$_{(aq)}$, to avoid the potential interference of TFA counterions during self-assembly. The metathesis quantitatively produced the expected salt, as confirmed by ^{19}F-NMR using α,α,α-trifluorotoluene as internal standard (see SI Section S5).

First, we analyzed the acid–base behavior of **V-FfFH$_2$**·2Cl at the molecular level in aqueous solution, to lay the basis for understanding its pH-responsive supramolecular behavior. The **VH**$^{2+}$ unit exhibits two π–π* bands characteristic of the protonated and deprotonated forms in the UV-vis spectra, thus enabling the spectroscopic determination of the pK_a^2 of the hydrazone group through pH-titration at a sufficiently low concentration of 20 μM **V-FfFH$_2$**·2Cl to avoid gelation (*vide infra*). In particular, the intensity of the main absorption band at λ_{max} = 378 nm, which is associated with the protonated form of the **VH**$^{2+}$ chromophore, decreases upon increasing the pH above 7. Conversely, at pH 7.5 there is the concomitant appearance of a new band at λ_{max} = 479 nm, which corresponds to the deprotonated form **V**$^+$, and its intensity increases at higher pH values (Fig. 1(b)). As a result, the titration revealed a pK_a^2 value of 9.0, in good agreement with previously reported data for other vermellogens.[37] Unfortunately, attempts to determine the pK_a^1 of the carboxylic acid group of the pseudopeptide C-terminus by potentiometric titrations with NaOH were unsuccessful due to the propensity of **V-FfFH$_2$**·2Cl to gel, as discussed below. To obtain a pK_a^1 estimate, a simplified dipeptide analogue with less gelation propensity was synthesized. The use of **V-fFH$_2$**·2Cl allowed to determine a pK_a^1 value of 3.3 at 0.7 wt% (7 mg mL^{-1}) for the carboxylic acid group (see SI Section S6), in good agreement with values for peptidic C-termini.[45] These results rule out a significant reciprocal influence of the two ionizable groups on the respective pK_a values, and establish suitable pH windows to study the potential changes of the gelation behavior of **V-FfFH$_2$**·2Cl (Fig. 1(c)).

2.2. V-FfFH$_2$·2Cl self-assembly into pH-responsive hydrogels

After the molecular characterization of the pseudopeptide and the estimation of the pK_a values of its two ionizable groups, we proceeded by studying its gelation behavior at different pH values, using 0.1 M aqueous phosphate buffer as a solvent. In the 1–6 pH range, in which **V-FfFH$_2$**·2Cl has 1 or 2 positive charges, the salt demonstrated high solubility in the buffer, without the need for sonication or heating of the samples, thereby offering a significant advantage in avoiding intermediate steps in hydrogelation protocols. **V-FfFH$_2$**·2Cl forms a gel at a minimum concentration of 0.4 wt% (4 mg mL^{-1}) after 30 min, although more stable and self-supportive hydrogels were obtained at 0.9 wt% (9 mg mL^{-1}) (Fig. 2(a)). Conversely, the simplified analog **V-fFH$_2$**·2Cl does not show the same behavior, indicating the requirement for at least three residues in the structure to achieve gelation. Oscillatory rheometry confirmed the stability and viscoelastic properties of the hydrogels in the pH range 1–6, with the elastic modulus G' higher than the viscous modulus G'', and both G' and G'' independent from the applied frequency in the range of 0.1–10 Hz, for samples at pH values within the range. Importantly, a pH-dependence of the viscoelastic properties was observed, showing variations in the average value of the elastic moduli (Fig. 2(b)), as well as differences in the gel resistance against applied stress (Fig. 2(c)). These results clearly show the influence of the net charge of the molecules on the viscoelastic properties of the hydrogels, with higher elastic moduli as the pH increases up to 6, the notable exception being the high G' value at pH 3. This peculiar behavior, together with the high resistance against applied stress observed at pH 3, suggests a higher degree of crosslinking of the hydrogel matrix when the pH is equal to the first pK_a^1 of the pseudopeptide, when the species **V-FfFH$_2$**$^{2+}$ and **V-FfFH**$^+$ are present in equimolar quantities. In contrast, at pH 7 and above, the pseudopeptide forms a red heterogeneous suspension, with complete precipitation at pH 10 (Fig. 2(a)). The aggregates formed in basic conditions are insoluble even after thermal treatment. This effect suggests that the self-assembled structures produced in acidic medium collapse as the pH approaches pK_a^2, and the zwitterionic form of the **V-FfF** compound, with net neutral charge, does not form hydrogels. Finally, the hydrogels formed between pH 1 and 6 are thermoreversible, exhibiting gel-to-sol transitions between 30 and 70 °C and fully recovering their structure upon cooling to room temperature (Fig. 2(a)). Their viscoelastic properties are likewise restored, with elastic moduli and stress-resistance values comparable to those measured prior to the thermal cycle (see SI Section S8).

2.3. Nanostructure characterization

Transmission electron microscopy (TEM) was used to correlate the macroscopic properties of **V-FfFH$_2$**·2Cl at different pH values with the corresponding nanostructures (Fig. 3 and SI Section S9). In the case of the gel obtained at pH = 1 (Fig. 3(a)), where the net charge is +2 (pH < pK_a^1), the matrix is constituted of long nanofibrillar bundles with an average diameter of 19.1 ± 2.2 nm (n = 120 counts), very similar to those observed in hydrogels obtained from other LMWPs forming amyloid structures.[46] As the pH increases to 2 (Fig. 3(b)) and 3 (Fig. 3(c)), the fibrils start to bundle into nanostructures that form nanoribbons (Fig. 3(g)), further closing up into nanotubes that become the predominant species at pH 4 (Fig. 3(d)), and persist at pH 5 (Fig. 3(e)) and 6 (Fig. 3(f)). To further support the proposed nanofiber-to-nanotube transition, we examined whether this morphological change could also be induced post-gelation. A hydrogel prepared at pH 1.5 was basified to pH 6 using a 1 M NaOH solution. TEM analysis of the initial acidic gel and of the same material after basification unequivocally confirmed the conversion of nanofibrils into nanotubes (see SI Section S11). This result demonstrates that the transition can be triggered solely by pH adjustment, even after gel formation, highlighting the dynamic nature of the supramolecular assembly.

We inferred that **V-FfFH**$^+$ is the species that self-assembles into nanotubes. At pH 3, corresponding to pK_a^1, the equimolar **V-FfFH**$^+$/**V-FfFH$_2$**$^{2+}$ mixture yields gels with the highest moduli

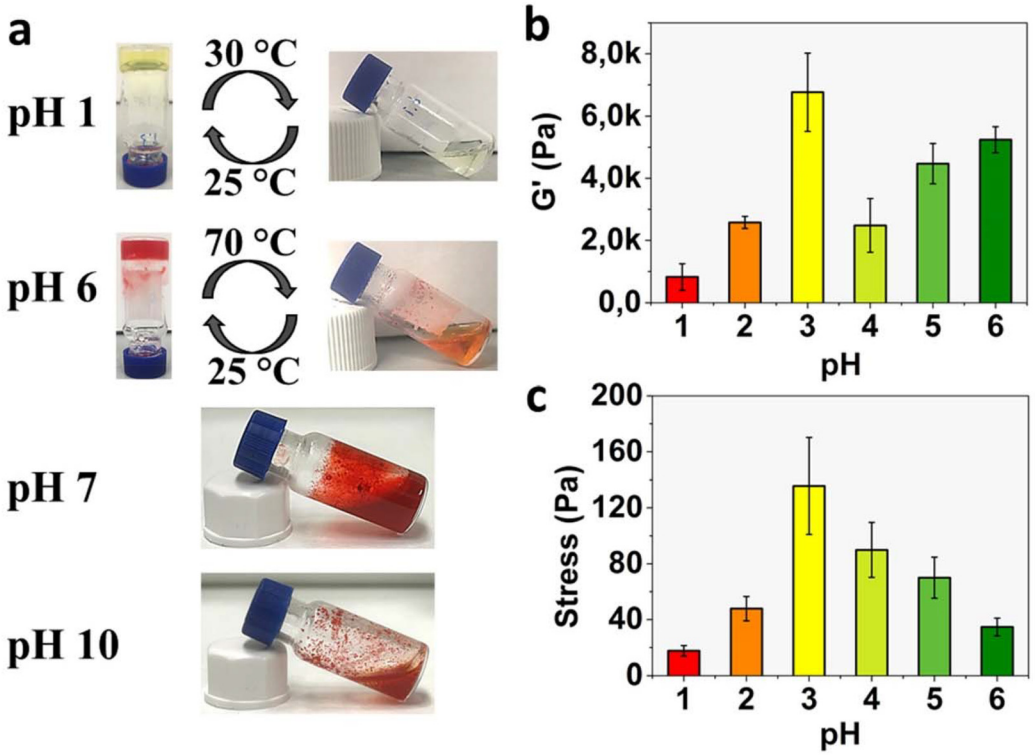

Fig. 2 (a) (From top to bottom) Hydrogels of **V-FfFH$_2$**·2Cl 0.9 wt% (9 mg mL^{-1}) at pH 1 and 6, and their gel-to-sol transition temperature. Heterogeneous system formed by **V-FfFH$_2$**·2Cl at pH 7. Precipitate formed by **V-FfFH$_2$**·2Cl at pH 10. (b and c) Viscoelastic properties of **V-FfFH$_2$**·2Cl in different buffer solutions. (b) Average values of elastic moduli (*G*′) obtained from frequency sweeps. (c) Average stress values corresponding to gel–sol transitions obtained from stress sweeps. All experiments were conducted in triplicate.

and resistance against applied stress (Fig. 2(b and c)), thanks to the ability of both nanostructures to interact with each other and entwine. Indeed, TEM micrographs showed fibrils running along nanotubes, suggesting an interconnection between the two nanostructures (Fig. S43), which may contribute to the increased elastic moduli and enhanced resistance to applied stress.

pH-dependent changes are also visible in the nanotube morphology. In particular, in the interval between pH = 3 and pH = 6 ($pK_a^1 \leq$ pH < pK_a^2), nanotubes are mostly single-walled (SW), with instances of double-walled (DW) and even triple-walled (TW) concentric nanotubes at pH 6 (insets in Fig. 3(d–f)), as it can be inferred by the uranyl acetate contrasting. The relative concentration of **V-FfFH$^+$** in the mixture has an interesting effect on the nanotube inner diameters: SW nanotubes at pH 3 have inner diameters of 5.5 ± 1.5 nm (n = 90 counts), while at pH 4–5 they reach their maximum width (21 ± 3.3 nm and 22 ± 3.9 nm (n = 50 counts each) at pH 4 and 5, respectively). At pH 6, the SW nanotube average diameter decreases to 17 ± 1.8 nm (n = 160 counts), together with the appearance of DW and TW nanotubes with average inner diameters of 14 ± 1.6 nm (n = 70 counts) and 9.5 ± 1.8 nm (n = 25 counts), respectively. Interestingly, the density of multi-walled (MW) nanotubes does not appear to depend directly on the gelator concentration, as doubling the concentration led to an increase in the density of SW nanotubes (Fig. 3(i)). A four-fold increase led to an even distribution of SW and DW nanotubes (50 ± 6.8%, $n \geq 75$) (Fig. 3(j)).

TEM and SEM analyses confirmed the heterogeneous morphology of the nanotubes at pH 6, ruling out the formation of sheets or other topologies (see SI, Sections S9 and S10). The presence of water channels in related peptide-containing nanofibers suggests that the transition from nanofibers to nanotubes – observed for **V-FfFH$^+$** gels between pH 1 and 3 – and the increase in nanotube surface area from pH 3 to 6,[47] are coupled with a widening of the water channels inside the nanotubes, until they collapse as the zwitterionic **V-FfF** form with net neutral charge appears.

2.4. Single-crystal X-ray diffraction and proposed nanotube model

After several unsuccessful attempts to obtain crystals of the pseudopeptide suitable for X-ray diffraction analysis in water solution at different pH values, needle crystals were obtained over a month from a gel in a methanol/water (50/50) mixture at pH 6. Their red colour indicated the deprotonation of the **V$^+$** unit in the pseudopeptide, as expected considering the formation of microcrystals of the zwitterionic form of **V-FfF** observed in TEM images (Fig. 3(h)). The compound crystallized in the triclinic crystal system, with space group *P*1. The

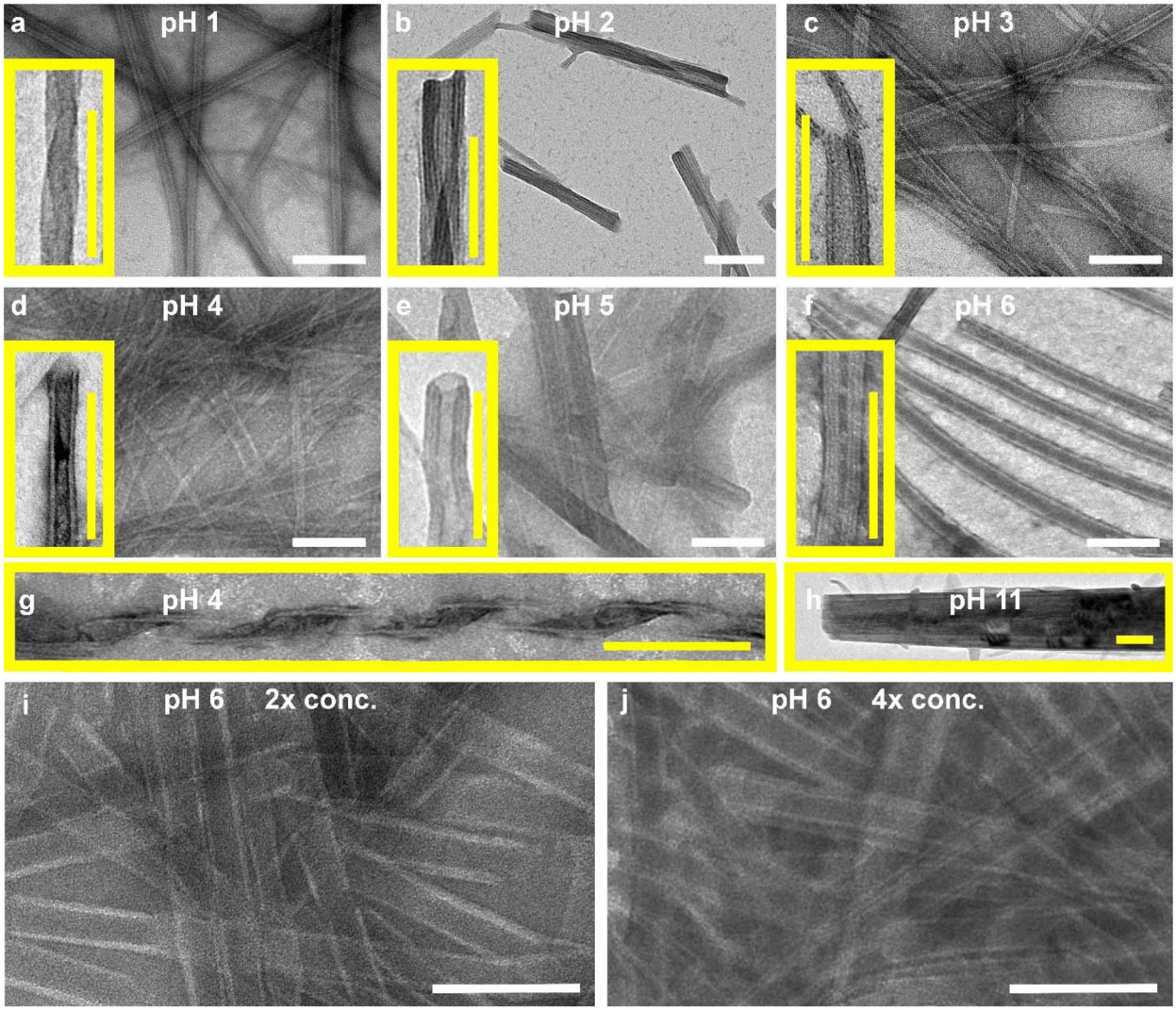

Fig. 3 TEM micrographs of the gels at pH 1 (a), pH 2 (b), pH 3 (c), pH 4 (d), pH 5 (e), and pH 6 at 0.9 wt% (9 mg mL^{-1}) (f), 1.7 wt% (17 mg mL^{-1}) (i), and 3.4 wt% (34 mg mL^{-1}) (j). Insets (2× magnification) show details of the nanostructures. (g) Shows a nanoribbon at pH 4. Scalebars = 100 nm. The nanostructures do not persist at pH ≥ 7 (not shown) and at pH 11 (h) microcrystals formed.

unit cell is constituted by two independent pseudopeptide molecules (green and cyan in Fig. 4), a methanol molecule with a statistical occupancy factor of 0.7, and two water molecules. As no counterions were located in the unit cell, the compound is expected to be zwitterionic. Disordered solvent molecules are present in the cavity between the hydrazone moieties.

The packing features alternating hydrophobic and hydrophilic layers, the former being composed of the three phenylalanine rings; the latter is formed by the peptidic backbone and the hydrazone moiety, which interact with the solvent. Both peptide conformers (cyan and green in Fig. 4(a)) display an overall curvature due to the heterochiral peptidic backbones, which, in the case of heterochiral dipeptides and tripeptides with phenylalanine residues, indeed arrange to form nanotubes with a hydrophilic inner surface.[47,48] Likewise, the peptide backbone interacts *via* hydrogen bonding through the amide groups in a parallel β-sheet motif (Fig. 4(b)), similarly to interactions found in the stacks that run along heterochiral dipeptide and tripeptide nanotubes.[47,48] We thus hypothesize that, also in the case of **V-FfFH$^+$**, the aromatic sidechains of the stacked peptides could form the hydrophobic walls, with the peptidic backbones providing the required curvature to form the cavity (Fig. 5(a)). A head-to-tail arrangement of five or six molecules forming the nanotube channel, as observed for heterochiral di- and tri-peptides (Fig. 5(b)), would indeed result in nanotubes with approximately 5 or 6 nm of inner diameter, which is the cavity dimension observed at pH 3 (Fig. 5(c) and SI Section S12). Wider nanotubes could arise from the head-to-tail arrangement of a higher number of pseudopeptides.

2.5. Secondary structure characterization of the pseudopeptide

In light of the formation of parallel stacks of the pseudopeptide, reminiscent of β-sheets, in the crystalline form of **V-FfF**,

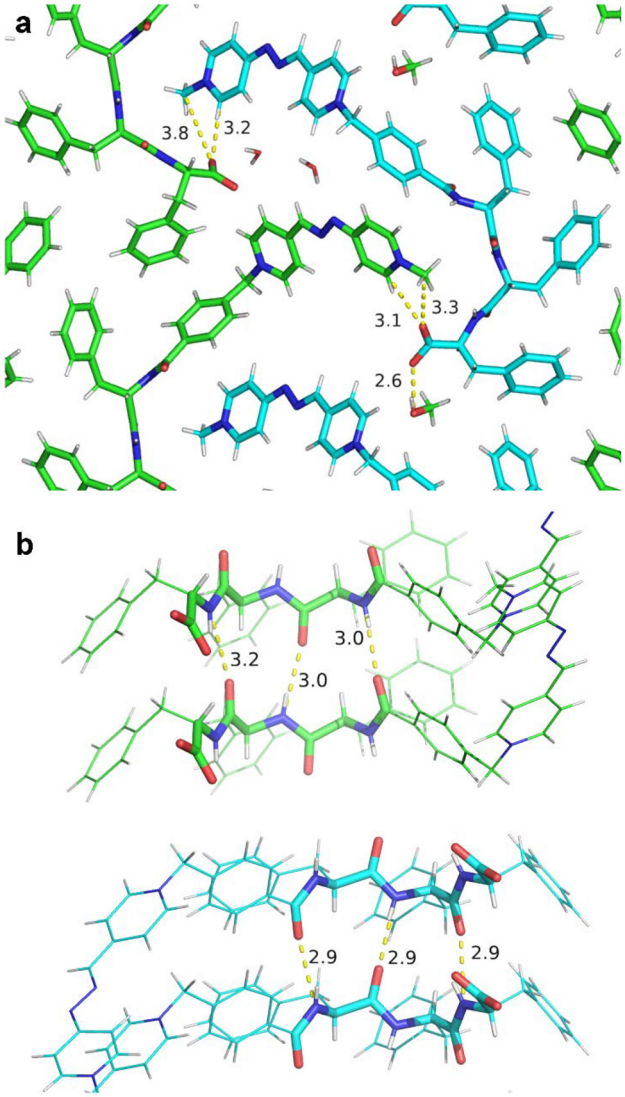

Fig. 4 Single-crystal XRD structure of **V-FfF** (CCDC 2420787). (a) Salt bridges between the C-terminal carboxylate and the *N*-methyl pyridinium moiety. (b) Hydrogen bonding between amide groups of the peptidic backbone holds together the stacks of the two conformers (green and cyan).

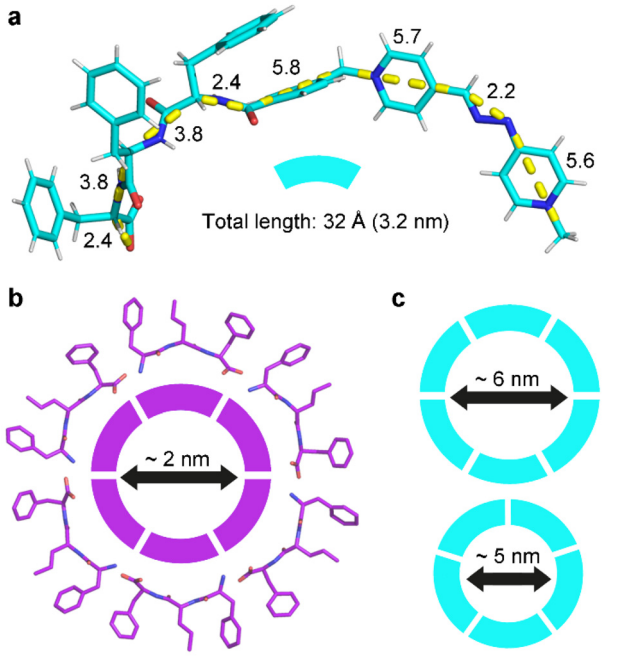

Fig. 5 (a) Molecular length of **V-FfF** calculated from the single-crystal XRD structure, and its cartoon representation. (b) Top-view of the crystal structure of the L-Phe-D-Nva-L-Phe heterochiral tripeptide forming a nanotube whose internal cavity is defined by 6 molecules, and its cartoon representation.[48] (c) Cartoon representation of the possible arrangements of **V-FfF** into nanotubes arising from 6 (top) or 5 (bottom) **V-FfF** molecules arranged head-to-tail, and their estimated internal diameter.

other spectroscopic techniques were used to ascertain the secondary structures adopted by the pseudopeptide in the gel. ATR-IR spectra were obtained in the pH range 1–6, showing the characteristic parallel β-sheet fingerprints in the amide-I region with signals between 1636 and 1632 cm^{-1} (Fig. S56).[49] Based on these observations, the main driving forces governing the self-assembly of the pseudopeptide are the hydrophobic effect associated with the triphenylalanine sequence, and the extensive intermolecular hydrogen bonding that stabilizes the parallel β-sheet arrangement. These interactions dominate independently of pH, meaning that both the nanofibers and the nanotubes are primarily composed of β-sheet-like assemblies.

To further corroborate these results, CD was used to obtain information on the secondary structure adopted by the pseudopeptides, analyzing the region between 190–230 nm, which corresponds to the n–π* and π–π* type transitions of the amides. However, at the concentration used in the study, 0.4 wt% (4 mg mL^{-1}), CD spectra could not be obtained due to the saturation of the dichroism signal. In contrast, the region corresponding to the π–π* transition of the protonated $\mathbf{VH}^{2+}$ moiety (300–450 nm) showed a bi-signed band in all pH conditions, from 1 to 6 (Fig. 6(a)), which is absent in solution and appears in **V-FfF**H_2·2Cl gels. This band, with positive and negative Cotton effects, is characteristic of an exciton coupling arising from the interaction of the excited states of a chromophore in a clockwise axial chirality environment.[50,51] Considering that the main secondary structure of **V-FfF**H_2·2Cl in the self-assembled material is reminiscent of a parallel β-sheet, we inferred that, in the pH range where the $\mathbf{VH}^{2+}$ moiety within the pseudopeptide carries two net positive charges, the aromatic moieties tilt to minimize electrostatic repulsions along the β-stack, resulting in the exciton coupling observed in the CD spectra. This hypothesis was further supported by SEM analyses, which revealed a clockwise helical arrangement in the nanofibers forming the hydrogel at pH = 1, thereby transferring chirality from the molecular level to the nanoscale (Fig. 6(b)). Moreover, this reorganization is also

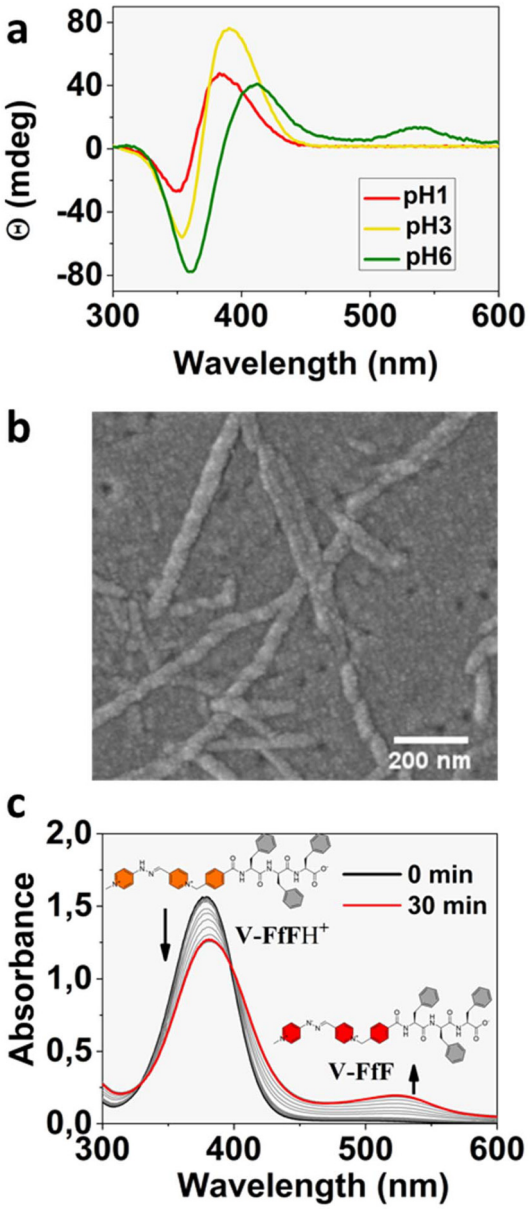

Fig. 6 (a) CD spectra recorded for the hydrogel 0.4 wt% (4 mg mL^{-1}) at pH 1, 3, and 6. (b) SEM image of the hydrogel at pH 1, showing the clockwise helical arrangement of the nanofibers. (c) Monitoring the hydrogelation of **V-FfFH**$^+$ 0.4 wt% (4 mg mL^{-1}) at pH 6 by UV-vis spectroscopy.

evident during the formation of the nanotubes, as one of the intermediates observed by TEM (Fig. 3(g)) corresponds to a helical-ribbon structure, thus reflecting the presence of axial chirality at the nanoscale.

Given the thermoreversible behavior observed at the macroscopic level (see above) and the strong excitonic band resulting from self-assembly, melting temperatures (T_m) of the hydrogels were determined by CD spectroscopy (see SI Section S14). In all hydrogels, the exciton coupling band progressively decreased with increasing temperature until it disappeared completely. Moreover, the T_m increased with pH, from 36 °C at pH 1 to 80 °C at pH 6, in good agreement with the macroscopic observations. UV-vis spectroscopy was used to monitor the hydrogel formation by deprotonation of the C-terminal acid group (pH 6), revealing a bathochromic shift in the absorption band associated with **VH**$^{2+}$ (Fig. 6(c)). As previously demonstrated with the analogue **VH**$^{2+}$ and related compounds,[37,52,53] this effect is associated with a hydrogen bonding interaction between the hydrazone group of the **VH**$^{2+}$ moiety and a hydrogen bonding acceptor, such as the deprotonated C-terminal acid of **V-FfFH**$^+$. These findings suggest that the transition from nanofibers to nanotubes is driven by a hydrogen-bonding interaction between the hydrazone group of one β-sheet and the deprotonated C-terminal of an adjacent β-sheet, in agreement with what had been proposed earlier based on the crystal structure (Fig. 5(c)). This lateral stacking between β-sheets provides an additional level of stabilization that promotes the evolution of nanofibers into nanotubes, a similar mechanism also observed in other systems that form nanotubes and whose nanostructure is modulated by pH.[54–56] On the other hand, a slight negative shift in pK_a[2] is observed upon aggregation, as reflected in the UV-vis and CD spectra at pH 6 (Fig. 6(a and c)), with the emergence of the π–π* band from the deprotonated form of the **V**$^+$ unit upon aggregation.

2.6. V-FfFH$_2$·2Cl hydrogel as a scaffold for controlled drug release

Skin cancer is one of the most common and aggressive types of cancer, with the potential to metastasize and lead to a fatal outcome. The microenvironment of melanoma cancer cells becomes acidic due to anaerobic glycolysis, down to a pH value between 6 and 6.7.[57] 5-fluorouracil (5-FU), a commonly used drug to treat this cancer, typically formulated in creams at concentrations of 1–5%, has limitations including poor penetration and skin damage.[58] Therefore, new encapsulation and delivery systems are being explored. Given the suitable mechanical and nanostructural properties of the pseudopeptide hydrogel at pH 6, it bears potential for its application as a controlled release platform for 5-FU.

Thus, the same gelling conditions described for the unloaded hydrogel were used to formulate the material with 5-FU as model cargo, mixing **V-FfFH**$_2$·2Cl at 0.8 wt% (8 mg mL^{-1}) with a solution of 5-FU (10 mg mL^{-1}) in phosphate buffer at pH = 6, which resulted in an orange suspension. After thermal solubilization of the components and subsequent cooling at 25 °C (r.t.), the 5-FU-loaded hydrogel with the same appearance as the unloaded one was obtained (Fig. S63). The viscoelastic properties of the 5-FU@**V-FfFH**$_2$·2Cl hydrogel showed a 5-fold increase in elastic modulus and a 3-fold increase in the yield of stress sweeps (Fig. S60), suggesting that the incorporation of 5-FU occurs through its interaction with the hydrogel matrix. Nanostructural characterization by TEM and SEM revealed the presence of nanotubes in the hydrogel (Fig. 7 and SI Fig. S61), similar but slightly larger than those observed without the drug. Characterization of the secondary structure of the loaded hydrogel by CD showed no change

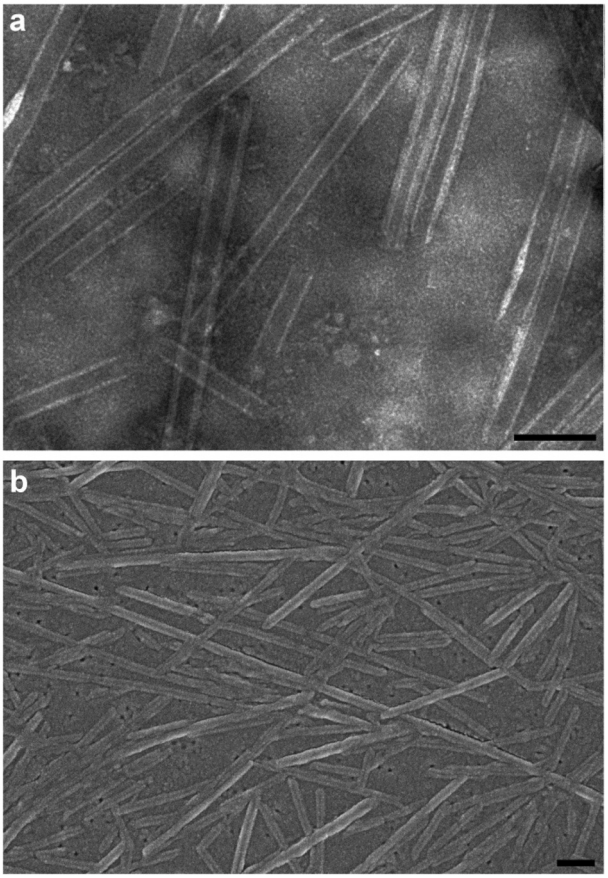

Fig. 7 Nanotubes of the pseudopeptide with 5-FU. (a) TEM micrograph, scalebar = 100 nm. (b) SEM image, scalebar = 300 nm.

compared to the unloaded material (Fig. S62). Release studies were conducted on the 5-FU-loaded hydrogel under physiological conditions at 37 °C, and the hydrogel was immersed in phosphate release buffer at pH 6, under sink conditions (see SI Section S17). The release of 5-FU was monitored by HPLC analyses of aliquots of the buffer taken at regular intervals. As shown in Fig. 8(a), during the first 8 hours, nearly 70% of the drug was gradually released. After 24 hours, the release reached a maximum of 87%, with no relevant changes after 72 hours. It is important to note that the hydrogel remained adhered to the bottom of the vial without showing any signs of degradation or swelling throughout the experiment, ensuring unidirectional diffusion of 5-FU into the release buffer. Therefore, based on the experimental conditions employed and considering the polymeric nature of the matrix, the semi-empirical kinetic model proposed by Ritger–Peppas for a diffusion-based release mechanism was applied.[59] As observed in the inset of Fig. 8(a), the plot of the initial 60% cumulative release *versus* the square root of time fits a straight line, confirming a Fickian diffusion process. Considering the high concentration of 5-FU compared to **V-FfFH**$^+$ and the observed release kinetics, it can be stated that there is a significant interaction between 5-FU and the hydrogel matrix. However,

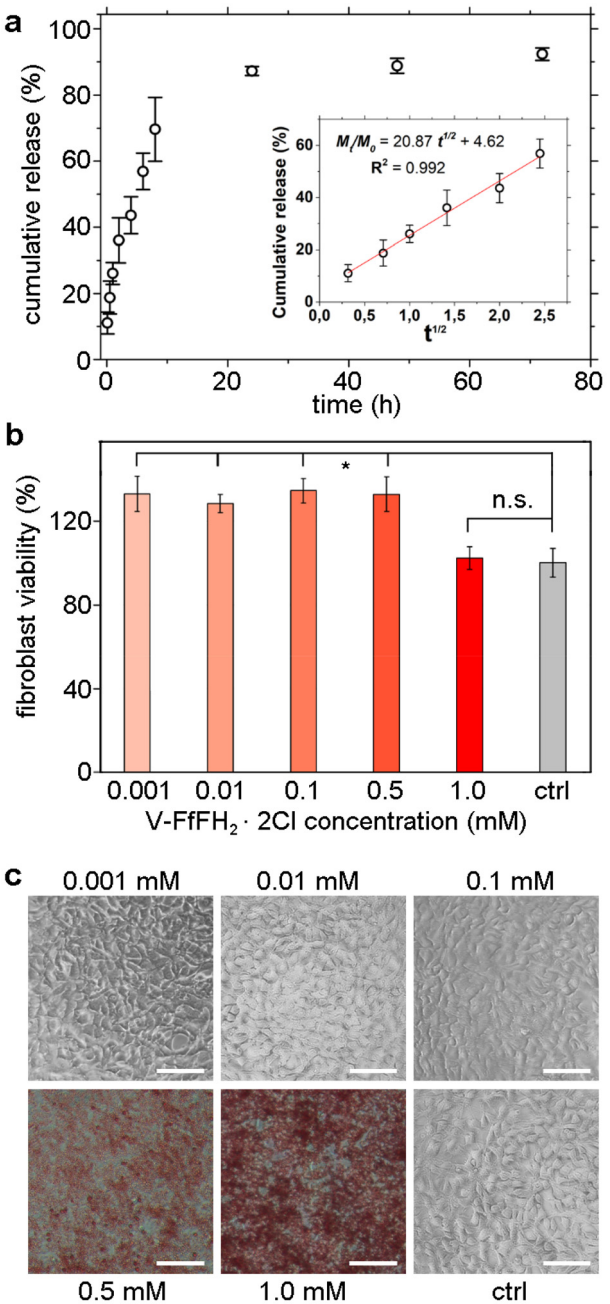

Fig. 8 (a) Cumulative release of 5-FU over 72 h. Inset: Plot of the initial 60% cumulative release *versus* the square root of time. (b and c) Viability of NIH-3T3 fibroblast cells in contact with different concentrations of **V-FfF**H$_2$·2Cl. *p < 0.005. Scalebars = 100 microns.

whether this interaction occurs exclusively with the surface of the nanotubes, without drug encapsulation, can neither be confirmed nor ruled out.

Finally, the cytotoxicity of **V-FfF**H$_2$·2Cl was evaluated in NIH-3T3 fibroblastic cells *in vitro*, using the WST-1 metabolic assay as a quantitative measure of cell proliferation in the presence of the compound, at concentrations ranging from 0.001 to 1 mM. As shown in Fig. 8(b), the WST-1 assays indicate

similar levels of metabolic activity at 1 mM of the compound, while at concentrations from 0.5 to 0.001 mM, a significant increase in metabolic activity and/or cell proliferation was observed. This slight decrease in cell viability observed at 1 mM of **V-FfF**H_2·2Cl is consistent with the compound's propensity to aggregate, as evidenced by the CD measurements at pH 7 (see SI Section S19), which indicate a CAC of approximately 0.75 mM. Additionally, phase contrast microscopy images evidenced the healthy cell morphology (Fig. 8(c) and SI Fig. S64), supporting the good cell viability in the presence of **V-FfF**H_2·2Cl. These results are also in good agreement with those previously reported for the non-peptidic $\mathbf{VH}^{2+}$ analogue in fibroblast cells.[37]

3. Conclusions

In this work, we present a novel dual pH-responsive pseudopeptidic hydrogelator (**V-FfF**H_2·2Cl), utilizing a heterochiral sequence of triphenylalanine (**FfF**) as the gelling unit and the first inherent pH-responsive unit, and "vermellogen" ($\mathbf{VH}^{2+}$) as a second pH-dependent molecular switch. The hydrogelator functions as a pH-adaptable platform, adjusting the viscoelastic properties of the material over a wide pH range (1 to 6), and undergoing reversible disassembly at pH above 7. Microscopic characterization of the hydrogel revealed a peculiar evolution from clockwise twisted nanofibers to nanotubes as a result of C-terminal deprotonation. This phenomenon is particularly remarkable as the resulting nanotubes exhibited an increase in internal diameter as the deprotonation of the C-terminal proceeded to completion. Furthermore, at pH 5–6, triple-walled and double-walled nanotubes were also detected by TEM analysis, and the relative concentration of the latter could be increased with increasing concentration of the pseudopeptide, demonstrating further tunability of this supramolecular nanostructured system. The potential biomedical applicability of **V-FfF**H_2·2Cl was evaluated, highlighting its high cytocompatibility with NIH-3T3 fibroblast cells and its ability to serve as a controlled release platform for the model drug (5-FU). These findings motivate us to explore further the peculiar controlled nanostructuration of the material for the development of advanced adaptive systems, where the observed evolution from nanofibers to nanotubes could have innovative and promising applications, such as in catalysis, functional surfaces, energy storage, or mechanical reinforcement.[60]

4. Experimental

4.1. Synthesis of V-FfF/fFH_2·2Cl

V-FfF/**fF**H_2·2TFA were synthesized following Fmoc-based SPPS with Oxyma-B activation. 2-Chlorotrityl chloride resin (1 g) was swollen in 10 mL of dichloromethane (DCM) for 30 min. 0.1 mL of $SOCl_2$ was added, and the mixture was stirred for 1 hour. The resin was washed with DCM (3 × 10 mL) and dimethylformamide (DMF, 3 × 10 mL). A solution of Fmoc-L-Phe-OH (620 mg, 1.6 mmol) and concentrated collidine (0.9 mL) in 15 mL of DMF was added to the resin and stirred for 1.5 hours. After that, 0.5 mL of MeOH was added, stirred for 10 min, and washed with DCM (3 × 10 mL) and DMF (3 × 10 mL). For the deprotection, a 20% piperidine in DMF was added (2 × 10 min), followed by washing with DCM (3 × 10 mL) and DMF (3 × 10 mL). For the first coupling, a solution of Fmoc-D-Phe-OH (1240 mg, 3.2 mmol), Oxyma-B (593 mg, 3.2 mmol), and *N*,*N*′-diisopropylcarbodiimide (DIC, 0.5 mL, 3.2 mmol) in 14 mL of DMF was prepared, added to the resin, and stirred for 1.5 hours. The resin was washed and deprotected as mentioned in the previous step. For the synthesis of compound **V-FfF**H_2·2TFA, a new coupling with Fmoc-L-Phe-OH and subsequent deprotection were carried out using the same steps described above. For the final coupling, a solution of **V**H·2PF_6 (2043 mg, 3.2 mmol, see SI for its synthesis), Oxyma-B (593 mg, 3.2 mmol), and DIC (0.5 mL, 3.2 mmol) in 18 mL of DMF was prepared, added to the resin, and stirred for 4 hours. After washing the resin with DCM and DMF, the pseudopeptide was cleaved from the resin by adding 10 mL of a solution of TFA, DCM, milliQ water, and TIPS (49 : 49 : 1 : 1). After 2 hours of stirring, the cleavage solution was concentrated under a stream of air to obtain a sticky red solid for both pseudopeptides. The solids were purified using HPLC (Agilent 1260 Infinity system) with a C-18 column (Kinetex, 5 μm, 100 Å, 250 × 10 mm, Phenomenex) and a gradient of acetonitrile (MeCN)/water with 0.05% TFA as follows: t = 0–3 min, 25% MeCN; t = 12 min, 95% MeCN; t = 15–20 min, 95% MeCN (R_t = 14–15 min and 9–10 min for **V-FfF**H_2·2TFA and **V-fF**H_2·2TFA respectively). For the metathesis to **V-FfF**/**fF**H_2·2Cl, the respective compound was dissolved at a concentration of 3.7 mM in a 10 mM aqueous solution of HCl, sonicated for 5 minutes, and then lyophilized. The metathesis reaction was monitored using ^{19}F-NMR, with α,α,α-trifluorotoluene employed as an internal standard, in a 1 : 8 molar ratio of peptide to internal standard (see SI Sections S4 and S5 for further details and characterization data).

4.2. pK_a determination

To determine the pK_a of the hydrazone group of **V-FfF**H_2·2Cl using UV-vis absorbance, a set of solutions at different pH values was prepared. The compound concentration was kept constant at 20 μM, and the phosphate buffer concentration was maintained at 0.1 M. Absorbance was read at 479 nm (see Section S6 for further details). Potentiometric pH titrations were performed by dissolving **V-fF**H_2·2Cl in Milli-Q water at 10 mM and subsequent additions of NaOH (0.5 M), and monitoring the pH with a pH-meter microelectrode (see SI Section S6 for further details).

4.3. Rheological data

Oscillatory rheology measurements were conducted using a Kinexus Ultra Plus instrument (Malvern, Alfatest, Italy), employing a parallel steel-plate geometry (20 mm) and Peltier cooling (25 °C). All hydrogels were prepared *in situ* just before

loading them into the rheometer. Measurement parameters for the time sweeps were set at 1 Hz and 1 Pa, for the frequency sweeps at 1 Pa, and for the stress sweeps at 1 Hz. All experiments were conducted in triplicate (see SI Section S7 for further details).

4.4. TEM analyses

Transmission electron microscopy (TEM) images were obtained using a Jeol JEM-2100 electron microscope (Japan) operating at 100 kV. Prior to imaging, 200-mesh copper grids coated with carbon (SPI, West Chester, USA) were rendered hydrophilic through exposure to UV-ozone (Procleaner Plus, USA) for 20 minutes. After allowing 1 hour for the self-organization of the pseudopeptide, approximately 3 μL of the hydrogel was carefully deposited onto the surface of the copper grid and left for 30 seconds. The excess sample was then removed by carefully blotting from a corner of the grid with a tissue for liquid absorption (Kemwipe, USA), and the grid was immediately placed in contact with 3 μL of 5% aqueous uranyl acetate for another 30 seconds. Finally, the grid was rinsed with the corresponding phosphate buffer and dried under vacuum. Image analysis was carried out using Image*J* software (see SI Section S9 for further details).

4.5. SEM analyses

Hydrogel samples were deposited on plastic coverslips and dried under vacuum. Samples were then mounted on aluminium stubs coated with double-sided carbon tape and sputter-coated with chromium using a Quorum Q150T ES plus sputter coater. Samples were analyzed with a Zeiss Gemini300 SEM working in secondary electron mode, at a working distance of 3 mm and with an acceleration voltage of 2 kV (see SI Section S10 for further details).

4.6. Crystallization

The pseudopeptide compound was dissolved at 1 mM in methanol and then diluted with water in a 50/50 final ratio. A small amount of sodium hydroxide solution was added to raise the pH value to 6. The solution turned from yellow to red, and gel aggregates formed. After one month, the gel aggregates evolved into red crystals. Single crystals were fished from the mother solution using cryo-loops and cryoprotected in NHV oil (Jena Bioscience, Germany). The loops were mounted on the goniometer and cooled down to 100 K (XRD1 beamline, Elettra synchrotron). For details on the X-ray diffraction data collection and analysis, see the SI, Section S12.

4.7. Drug release

A mixture of 5-FU (20 mg) and **V-FfF**H_2·2Cl (17.3 mg) was prepared in 2 mL of phosphate buffer at pH 6 (0.1 M). 0.5 mL of the mixture was placed in a 10 mL vial (5 mg of 5-FU and 4.3 mg of **V-FfF**H_2·2Cl) and heated in a silicone bath at 70 °C until complete solubilization (3 replicates were prepared). The solution was allowed to cool down to room temperature until the hydrogel formed at the bottom of the vial, covering it homogeneously. After 24 hours, 8 mL of phosphate buffer at pH 6 was very carefully pipetted along the vial glass, avoiding disruption of the hydrogel. Subsequently, the three replicates were placed in a heated shaker at 37 °C, with mild agitation set at 60 rpm. For the analysis of the released 5-FU, 50 μL of buffer release was taken at each time point for HPLC analysis and replaced with fresh buffer. See SI, Section S17 for further details.

4.8. Cell viability experiments

NIH-3T3 cells (Life Sciences Dept., University of Trieste, Italy) were routinely grown in Dulbecco's modified Eagle's medium (DMEM, Sigma Aldrich, Missouri, United States) supplemented with 100 μg mL^{-1} streptomycin, 100 unit per mL penicillin, and 10% (v/v) heat-inactivated fetal bovine serum. Cells were maintained at 37 °C in a saturated humidity atmosphere containing 5% CO_2 in 25 cm^2 flasks. The cytocompatibility of different concentrations of **V-FfF**H_2·2Cl was assayed using the WST-1 assay (Roche; Basel, Switzerland). NIH-3T3 cells were cultured in a 96-well microplate (tissue-culture grade, clear, flat bottom; Sarstedt, Numbrecht, Germany) at a seeding density of 10 000 cells per well in 100 μL of supplemented DMEM for 24 hours in a controlled atmosphere. Then, the media was removed, the cells were washed with PBS, and 100 μL of a solution at 0.001 mM, 0.01 mM, 0.1 mM, 0.5 mM, or 1 mM of **V-FfF**H_2·2Cl dissolved in supplemented DMEM was added per well. To the control wells, only supplemented DMEM was added. Cells were incubated for another 24 hours in a controlled atmosphere. The next morning, cell morphology was inspected using phase contrast microscopy, and right after 5 μL of WST-1 reagent was added to each well. After 2 h of incubation, absorbance at 450 nm was measured with a microplate reader (Synergy H1, BioTek, Winooski, United States). Each condition was repeated in 5 replicas, and statistical analysis was performed in Excel using the *t*-test; $p < 0.005$ was used as the reference value for statistical significance.

Author contributions

The manuscript was written through the contribution of all authors. All authors have approved to the final version of the manuscript.

Conflicts of interest

There are no conflicts to declare.

Data availability

The data supporting this article have been included as part of the supplementary information (SI). Supplementary information is available. See DOI: https://doi.org/10.1039/d5nr04076k.

CCDC 2420787 contains the supplementary crystallographic data for this paper.[61]

Acknowledgements

The authors are grateful for the funding received from the MCIN/AEI/10.13039/501100011033 and ERDF *A way of making Europe* (PID2022-137361NB-I00), the Consellería de Cultura, Educación e Universidade da Xunta de Galicia (ED431C 2022/39). A. B.-G. thanks the Consellería de Cultura, Educación e Universidade da Xunta de Galicia for his postdoctoral fellowships (ED481D-2024-020). S. M. acknowledged funding from the Italian Ministry of University and Research through the PRIN program (SHAZAM project, grant no. 2022XEZK7K) funded by the European Union – NextGenerationEU. This research was also funded by the Slovenian Research and Innovation Agency (ARIS) through the core funding No. P2-0089, ARIS projects: No. J2-60047, J2-3043, J3-3079, J7-4420, L2-60141. The authors acknowledge the CEMM Nanocenter (JSI, Slovenia) for the access to electron microscopy, and Dr Maurizio Polentarutti and the Elettra Synchrotron (Trieste) for the XRD data collection at the XRD1 beamline.

References

1 M. Amit, S. Yuran, E. Gazit, M. Reches and N. Ashkenasy, *Adv. Mater.*, 2018, **30**, 1707083.
2 A. Dasgupta and D. Das, *Langmuir*, 2019, **35**, 10704.
3 N. Mahmoudi, Y. Wang, N. Moriarty, N. Y. Ahmed, N. Dehorter, L. Lisowski, A. R. Harvey, C. L. Parish and R. J. Williams, *ACS Nano*, 2024, **18**, 3597.
4 K. Tao, A. Levin, L. Adler-Abramovich and E. Gazit, *Chem. Soc. Rev.*, 2016, **45**, 3935.
5 A. D. Martin and P. Thordarson, *J. Mater. Chem. B*, 2020, **8**, 863.
6 P. J. Jervis, C. Amorim, T. Pereira, J. A. Martins and P. M. T. Ferreira, *Soft Matter*, 2020, **16**, 10001.
7 J. Mitrovic, G. Richey, S. Kim and M. O. Guler, *Langmuir*, 2023, **39**, 11935.
8 E. Radvar and H. S. Azevedo, *Macromol. Biosci.*, 2018, **19**, 1800221.
9 I. W. Hamley, *ACS Appl. Bio Mater.*, 2023, **6**, 384.
10 N. Mahmoudi, E. Mohamed, S. S. Dehnavi, L. M. Caballero-Aguilar, A. R. Harvey, C. L. Parish, R. J. Williams and D. R. Nisbet, *Adv. Sci.*, 2024, **11**, 2303707.
11 C. Diaferia, G. Morelli and A. Accardo, *J. Mater. Chem. B*, 2019, **7**, 5142.
12 D. Giuri, P. Ravarino and C. Tomasini, *Org. Biomol. Chem.*, 2021, **19**, 4622.
13 N. Balasco, D. Altamura, P. L. Scognamiglio, T. Sibillano, C. Giannini, G. Morelli, L. Vitagliano, A. Accardo and C. Diaferia, *Langmuir*, 2024, **40**, 1470.
14 M. Reches and E. Gazit, *Science*, 2003, **300**, 625.
15 X. Yan, P. Zhu and J. Li, *Chem. Soc. Rev.*, 2010, **39**, 1877.
16 M. Yemini, M. Reches, E. Gazit and J. Rishpon, *Anal. Chem.*, 2005, **77**, 5155.
17 S. Safaryan, V. Slabov, S. Kopyl, K. Romanyuk, I. Bdikin, S. Vasilev, P. Zelenovskiy, V. Y. Shur, E. A. Uslamin, E. A. Pidko, A. V. Vinogradov and A. L. Kholkin, *ACS Appl. Mater. Interfaces*, 2018, **10**, 10543.
18 K. Tao, P. Makam, R. Aizen and E. Gazit, *Science*, 2017, **358**, eaam9756.
19 S. Kralj, O. Bellotto, E. Parisi, A. M. García, D. Iglesias, S. Semeraro, C. Deganutti, P. D'Andrea, A. V. Vargiu, S. Geremia, R. De Zorzi and S. Marchesan, *ACS Nano*, 2020, **12**, 16951.
20 W. Ji, C. Q. Yuan, P. Chakraborty, S. Makam, S. Bera, S. Rencus-Lazar, J. B. Li, X. H. Yan and E. Gazit, *ACS Nano*, 2020, **14**, 7181.
21 V. Devika, P. J. Sreelekshmi, N. Rajeev, A. S. Lakshmi, A. Chandran, G. B. Gouthami and S. Sadanandan, *Mol. Pharm.*, 2022, **19**, 1999.
22 M. E. Roth-Konforti, M. Comune, M. Halperin-Sternfeld, I. Grigoriants, D. Shabat and L. Adler-Abramovich, *Macromol. Rapid Commun.*, 2018, **39**, 1800588.
23 S. Adorinni, G. Goti, L. Rizzo, F. Grassi, S. Kralj, F. Matroodi, M. Natali, R. De Zorzi, S. Marchesan and L. Dell'Amico, *Chem. Commun.*, 2023, **59**, 7619.
24 T. Miyata, M. Jige, T. Nakaminami and T. Uragami, *Proc. Natl. Acad. Sci. U. S. A.*, 2006, **103**, 1190.
25 Z. Li, Y. Zhu and J. B. Matson, *ACS Appl. Bio Mater.*, 2022, **5**, 4635.
26 A. Aggeli, M. Bell, N. Boden, L. M. Carrick and A. E. Strong, *Angew. Chem., Int. Ed.*, 2003, **42**, 5603.
27 C. Diaferia, N. Balasco, D. Altamura, T. Sibillano, E. Gallo, V. Roviello, C. Giannini, G. Morelli, L. Vitagliano and A. Accardo, *Soft Matter*, 2018, **14**, 8219.
28 L. Mei, K. Xu, Z. Zhai, S. He, T. Zhu and W. Zhong, *Org. Biomol. Chem.*, 2019, **17**, 3853.
29 C. Schiattarella, C. Diaferia, E. Gallo, B. Della Ventura, G. Morelli, L. Vitagliano, R. Velotta and A. Accardo, *Sci. Rep.*, 2022, **12**, 759.
30 S. Adorinni, S. Gentile, O. Bellotto, S. Kralj, E. Parisi, M. C. Cringoli, C. Deganutti, G. Malloci, F. Piccirilli, P. Pengo, L. Vaccari, S. Geremia, A. V. Vargiu, R. De Zorzi and S. Marchesan, *ACS Nano*, 2024, **18**, 3011.
31 C. Diaferia, E. Gianolio, T. Sibillano, F. A. Mercurio, M. Leone, C. Giannini, N. Balasco, L. Vitagliano, G. Morelli and A. Accardo, *Sci. Rep.*, 2017, **7**, 307.
32 M. A. Elsawy, J. K. Wychowaniec, L. A. Castillo Díaz, A. M. Smith, A. F. Miller and A. Saiani, *Biomacromolecules*, 2022, **23**, 2624.
33 A. Blanco-Gómez, Á. Fernández-Blanco, V. Blanco, J. Rodríguez, C. Peinador and M. D. García, *J. Am. Chem. Soc.*, 2019, **141**, 3959.
34 A. Blanco-Gómez, I. Neira, J. L. Barriada, M. Melle-Franco, C. Peinador and M. D. García, *Chem. Sci.*, 2019, **10**, 10680.
35 P. Cortón, H. Wang, I. Neira, A. Blanco-Gómez, E. Pazos, C. Peinador, H. Li and M. D. García, *Org. Chem. Front.*, 2022, **9**, 81.

36 P. Cortón, N. Fernández-Labandeira, M. Díaz-Abellás, C. Peinador, E. Pazos, A. Blanco-Gómez and M. D. García, *J. Org. Chem.*, 2023, **88**, 6784.
37 L. Barravecchia, A. Blanco-Gómez, I. Neira, R. Skackauskaite, A. Vila, A. Rey-Rico, C. Peinador and M. D. García, *J. Am. Chem. Soc.*, 2022, **144**, 19127.
38 L. Barravecchia, I. Neira, E. Pazos, C. Peinador and M. D. García, *J. Org. Chem.*, 2022, **87**, 760.
39 M. A. García, M. Kurbasic, S. Kralj, M. Melchionna and S. Marchesan, *Chem. Commun.*, 2017, **53**, 8110.
40 M. C. Cringoli, C. Romano, E. Parisi, L. J. Waddington, M. Melchionna, S. Semerano, R. De Zorzi, M. Grönholm and S. Marchesan, *Chem. Commun.*, 2020, **56**, 3015.
41 A. M. García, R. Lavendomme, S. Kralj, M. Kurbasic, O. Bellotto, M. C. Cringoli, S. Semeraro, A. Bandiera, R. De Zorzi and S. Marchesan, *Chem. – Eur. J.*, 2020, **26**, 1880.
42 A. M. García, M. Melchionna, O. Bellotto, S. Kralj, S. Semeraro, E. Parisi, D. Iglesias, P. D'Andrea, R. De Zorzi, A. V. Vargiu and S. Marchesan, *ACS Nano*, 2021, **15**, 3015.
43 Y. Ozawa, H. Sato, Y. Kayano, N. Yamaki, Y. Izato, A. Miyake, A. Naito and I. Kawamura, *Phys. Chem. Chem. Phys.*, 2019, **21**, 10879.
44 I. G. R. Gutz, CurTiPot, 2022, https://www.iq.usp.br/gutz/Curtipot_.html (accessed July 20, 2025).
45 C. Tanford, *Adv. Protein Chem.*, 1968, **23**, 121.
46 O. S. Makin and L. C. Serpell, *FEBS J.*, 2005, **272**, 5950.
47 O. Bellotto, P. D'Andrea and S. Marchesan, *J. Mater. Chem. B*, 2023, **11**, 5378.
48 A. M. García, D. Iglesias, E. Parisi, K. E. Styan, L. J. Waddington, C. Deganutti, R. De Zorzi, M. Grassi, M. Melchionna, A. T. Vargiu and S. Marchesan, *Chem*, 2018, **4**, 1862.
49 P. W. J. M. Frederix, G. G. Scott, Y. M. Abul-Haija, D. Kalafatovic, C. G. Pappas, N. Javid, N. T. Hunt, R. V. Ulijn and T. Tuttle, *Nat. Chem.*, 2015, **7**, 30.
50 Y. Ma, X. Cheng, H. Ma, Z. He, Z. Zhang and W. Zhang, *Chem. Sci.*, 2022, **13**, 13623.
51 J. Kwon, K. H. Park, W. J. Choi, N. A. Kotov and J. Yeom, *Acc. Chem. Res.*, 2023, **56**, 1359.
52 H. Wang, S. Fang, G. Wu, Y. Lei, Q. Chen, H. Wang, Y. Wu, C. Lin, X. Hong, S. K. Kim, J. L. Sessler and H. Li, *J. Am. Chem. Soc.*, 2020, **142**, 20182.
53 M. Boiocchi, L. Del-Boca, D. Esteban-Gómez, L. Fabbrizzi, M. Licchelli and E. Monzani, *J. Am. Chem. Soc.*, 2004, **126**, 16507.
54 S. Wang, F. Liu, N. Ma, Y. Li, Q. Jing, X. Zhou and Y. Xia, *Nanoscale*, 2021, **13**, 13318.
55 H. Xu, Y. M. Wang, X. Ge, S. Y. Han, S. J. Wang, P. Zhou, H. H. Shan, X. B. Zhao and J. A. R. Lu, *Chem. Mater.*, 2010, **22**, 5165.
56 E. Pouget, E. Dujardin, A. Cavalier, A. Moreac, C. Valery, V. Marchi-Artzner, T. Weiss, A. Renault, M. Paternostre and F. Artzner, *Nat. Mater.*, 2007, **6**, 434.
57 J. L. Wike-Hooley, J. Haveman and H. S. Reinhold, *Radiother. Oncol.*, 1984, **2**, 343.
58 J. J. Lee, J. H. Beumer and E. Chu, *Cancer Chemother. Pharmacol.*, 2016, **78**, 447.
59 P. L. Ritger and N. A. Peppas, *J. Controlled Release*, 1987, **5**, 23.
60 T. Shimizu, W. Ding and N. Kameta, *Chem. Rev.*, 2020, **120**, 2347.
61 CCDC 2420787: Experimental Crystal Structure Determination, 2026, DOI: 10.5517/ccdc.csd.cc2m80xv.